

ARTICLE TYPE

An asynchronous variational integrator for the phase field approach to dynamic fracture

Zongwu Niu¹ | Vahid Ziaei-Rad^{1,3} | Zongyuan Wu¹ | Yongxing Shen^{*1,2}

¹University of Michigan – Shanghai Jiao Tong University Joint Institute, Shanghai Jiao Tong University, Shanghai, China

²Shanghai Key Laboratory for Digital Maintenance of Buildings and Infrastructure, Shanghai, China

³Department of Environmental Informatics, Helmholtz Centre for Environmental Research – UFZ, Leipzig, Germany

Correspondence

*Yongxing Shen, University of Michigan – Shanghai Jiao Tong University Joint Institute, Shanghai Jiao Tong University, Shanghai 200240, China. Email: yongxing.shen@sjtu.edu.cn

Summary

The phase field approach is widely used to model fracture behaviors due to the absence of the need to track the crack topology and the ability to predict crack nucleation and branching. In this work, the asynchronous variational integrators (AVI) is adapted for the phase field approach of dynamic brittle fractures. The AVI is derived from Hamilton's principle and allows each element in the mesh to have its own local time step that may be different from others'. While the displacement field is explicitly updated, the phase field is implicitly solved, with upper and lower bounds strictly and conveniently enforced. In particular, the AT1 and AT2 variants are equally easily implemented. Three benchmark problems are used to study the performances of both AT1 and AT2 models and the results show that AVI for phase field approach significantly speeds up the computational efficiency and successfully captures the complicated dynamic fracture behavior.

KEYWORDS:

phase field approach, asynchronous variational integrators, dynamic fracture, computational efficiency

1 | INTRODUCTION

Dynamic fracture refers to crack development processes accompanied by fast changes in applied loads and rapid crack propagation, where inertial forces play an important role during the evolution. Application examples of dynamic fracture include drop tests of electronic devices, oil exploitation, and impact on vehicles.

Dynamic fracture of solids has been extensively studied^{1,2,3,4}. Over the past decades, various numerical methods⁵ to simulate dynamic fracture have been proposed, which can be classified into two groups: discrete approaches and smeared-crack ones. A discrete approach explicitly describes the crack topology, such as the extended finite element method⁶, cohesive zone model⁷, element deletion method⁸, cracking element method⁹, and phantom nodes method¹⁰, just to name a few in the context of dynamic fracture. Conversely, a smeared-crack approach represents the crack by a smeared crack band, which includes the gradient damage model¹¹, the thick level set approach¹², and so on.

The regularized variational fracture method¹³, also called the phase field method for fracture, belongs to the group of smeared-crack approaches. It originates from Griffith's energetic theory and was developed based on the variational approach to brittle fracture by Francfort and Marigo¹⁴. The formulation solves crack problems by minimizing an energy functional that consists of the elastic energy, external work, and the crack surface energy. This way, crack evolution is a natural outcome of the solution. The phase field method possesses the following advantages: (1) the crack evolves naturally and there is no need of a crack tracking algorithm; (2) there is no need of additional criterion for crack branching and merging; (3) the implementation is straightforward even for complicated crack problems in 3D. These advantages facilitate its application for various fracture problems, such as

17 shell fracture¹⁵, beam fracture¹⁶, and carbon dioxide fracturing¹⁷. For details about the implementation of this approach, we
18 refer the reader to the work by Shen et al.¹⁸

19 For dynamic fracture, Borden et al.¹⁹ combined the phase field method with isogeometric analysis with local adaptive refine-
20 ment to simulate dynamic brittle fracture. Nguyen and Wu²⁰ presented a phase field regularized cohesive zone model for dynamic
21 brittle fracture. Hao et al.^{21,22} developed formulations for high-speed impact problems for metals, accounting for volumetric and
22 shear fractures.

23 However, the phase field model suffers from high computational cost partly because of the small critical time step, which, in
24 turn, results from the necessary fine spatial discretization near the crack to resolve the regularization length scale. In order to
25 overcome this challenge, various schemes to accelerate such computation have been proposed. Tian et al.²³ presented a multilevel
26 hybrid adaptive finite element phase field method for quasi-static and dynamic brittle fracture, wherein the refinement is based on
27 the crack tip identified with a certain scheme. Ziaei-Rad and Shen²⁴ developed a parallel algorithm on the graphical processing
28 unit with time adaptivity strategy to speed up the computation. Li et al.²⁵ proposed a variational h-adaptation method with both a
29 mesh refinement and a coarsening scheme based on an energy criterion. Engwer et al.²⁶ proposed a linearized staggered scheme
30 with dynamic adjustments of the stabilization parameters throughout the iteration to reduce the computational cost.

31 In this work, with the aim of accelerating dynamic phase field fracture computations, we adapt the asynchronous variational
32 integrator (AVI) for this problem. The AVI is an instance of variational integrators. Variational integrators are a class of time
33 integration algorithms derived from Hamilton's principle of stationary action and have the advantages of symplectic-momentum
34 conservation and remarkable energy (or Hamiltonian) behavior for long-time integration. In essence, they can be classified into
35 synchronous variational integrators and asynchronous variational integrators. The former, such as central difference, requires
36 all unknown variables to be solved with the same time step, taking into account global requirement of stability and accuracy.

37 In contrast, the latter allows independent time steps for each term contributing to the action functional, effectively independent
38 time steps for each element in the context of finite elements. This asynchrony allows the elements with smaller time steps to be
39 more frequently updated. Moreover, the method may be made fully explicit and even in the implicit case, only assembly of local
40 reaction forces and stiffness matrices instead of global ones is needed. For linear elastodynamics, the AVI was first introduced
41 by Lew et al.^{27,28}, and the stability and convergence of AVI have been proved by Fong et al.²⁹ and by Focardi and Mariano³⁰,
42 respectively. In addition, the AVI has been extended to the contact problem³¹, wave propagation³² and computer graphics³³.

43 In the case of AVI for the phase field approach to fracture, a few adjustments need to be made. First and foremost, the overall
44 Lagrangian is free of the time derivative of the phase field; hence solving the phase field is a local steady-state problem. More
45 precisely, the coupled multi-field system is solved by employing a staggered scheme, in which the displacement and velocity
46 fields are integrated with an explicit scheme while the phase field is the solution of an inequality-constrained optimization
47 problem. In essence, the phase field of only one element is solved at a time, for which it is very convenient to enforce the inequality
48 constraint compared to doing so for the entire domain. This feature allows implementing the AT1 variant of the method³⁴ with
49 a similar cost for the more widely used AT2 variant.

50 There are other asynchronous methods for dynamic fracture with the phase field. For example, Ren et al.³⁵ proposed an
51 explicit phase field formulation where the mechanical field is solved with a larger time step while the phase field is updated with
52 smaller sub-steps. Suh and Sun³⁶ presented a subcycling method to capture the brittle fracture in porous media, where the heat
53 transfer between the fluid and solid constituents is solved with different time steps as integer multiples of each other. Note that
54 the methods in Refs. 35,36 are not variational, hence may not enjoy the said advantages of variational integrators.

55 The paper is organized as follows. In Section 2, we briefly review the formulation of the phase field model for brittle fracture
56 and introduce Hamilton's principle in the continuum Lagrangian framework. In Section 3, we present the asynchronous space-
57 time discretization scheme and derive discrete Euler-Lagrange equations by discrete variational principle, then we present how
58 to solve the mechanical field and phase field by a staggered scheme. In addition, we summarize the overall implementation of
59 AVI for the phase field approach to fracture. In Section 4, we showcase three benchmark examples under dynamic loading for
60 verification and examining the performance. Finally, we conclude this work in Section 5.

61 2 | FORMULATIONS

62 This section devotes to the formulation of a dynamic fracture phase field model through Hamilton's principle for an elastic body
63 with possible cracks represented by a phase field.

64 2.1 | Hamilton's principle

Let $\Omega \subset \mathbb{R}^n$, $n = 2, 3$, be the domain occupied by the reference configuration of a body with possible cracks. Hamilton's principle states that the true trajectory of a body with prescribed initial and final conditions is the stationary point of the action functional with respect to arbitrary admissible variations. Here, we consider Ω with possible internal cracks during a specified time interval $t \in [t_0, t_f]$ with the action functional given by

$$S(\mathbf{u}, d) = \int_{t_0}^{t_f} L(\mathbf{u}, \dot{\mathbf{u}}, d) dt, \quad (1)$$

where $\mathbf{u}(\mathbf{X}, t)$, $\mathbf{X} \in \Omega$, denotes the displacement field of the body, and $\dot{\mathbf{u}} = d\mathbf{u}/dt$ is the velocity field. The scalar field $d : \Omega \times [t_0, t_f] \rightarrow [0, 1]$ is called the phase field, which approximates possible sharp cracks in a diffusive way. Herein, the Lagrangian function is in the form

$$L(\mathbf{u}, \dot{\mathbf{u}}, d) = T(\dot{\mathbf{u}}) - V(\mathbf{u}, d) - \Gamma(d), \quad (2)$$

where $V(\mathbf{u}, d)$ is the potential energy, $\Gamma(d)$ is the crack surface energy, and

$$T(\dot{\mathbf{u}}) = \int_{\Omega} \frac{1}{2} \rho \dot{\mathbf{u}} \cdot \dot{\mathbf{u}} d\Omega \quad (3)$$

65 is the kinetic energy, where ρ is the initial mass density.

66 2.2 | Phase field approximation

In this subsection, we revisit the two versions of the phase field model as a basis for subsequent development. In the phase field model of fracture, the sharp crack surface is approximated by a scalar phase field d as shown in Figure 1. The range of this field d has to be between 0 and 1. In particular, our convention is such that the region with $d = 1$ represents the fully cracked state and that with $d = 0$ represents the pristine state of the material. Following Ref. 13, the crack surface energy $\Gamma(d)$ in (2) is given by

$$\Gamma(d) = \int_{\Omega} g_c \gamma(d, \nabla d) d\Omega, \quad (4)$$

where $g_c > 0$ is the critical crack energy release rate, and $\gamma(d, \nabla d)$ is the crack surface density per unit volume,

$$\gamma(d, \nabla d) = \frac{1}{4c_w} \left(\frac{w(d)}{\ell} + \ell |\nabla d|^2 \right), \quad (5)$$

67 where $\ell > 0$ is the regularization length scale parameter, which controls the width of the transition region of the smoothed
 68 crack. Crack geometric function $w(d)$ and normalization constant $c_w = \int_0^1 \sqrt{w(d)} dd$ are model dependent. Specifically, for
 69 the brittle fracture, classical examples are $w(d) = d^2$ and $c_w = 1/2$ for the AT2 model; and $w(d) = d$ and $c_w = 2/3$ for the
 70 AT1 model³⁴. In addition, a notable difference between the AT2 and AT1 models is that the former gives rise to a more diffuse
 71 phase field profile while the latter generates a phase field profile with a narrow support near the crack.

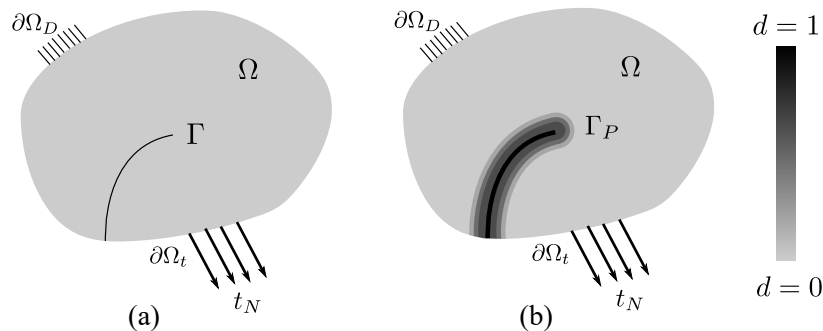


FIGURE 1 Body with an internal crack with: (a) a sharp crack; (b) a crack approximated by the phase field.

The potential energy $V(\mathbf{u}, d)$ in (2) is expressed as

$$V(\mathbf{u}, d) = \int_{\Omega} \psi(\boldsymbol{\varepsilon}(\mathbf{u}), d) d\Omega - \int_{\partial\Omega_t} \mathbf{t}_N \cdot \mathbf{u} dA - \int_{\Omega} \mathbf{b} \cdot \mathbf{u} d\Omega, \quad (6)$$

where ψ is the strain energy density, $\mathbf{t}_N : \partial\Omega_t \rightarrow \mathbb{R}^n$ is the prescribed traction boundary condition, and $\mathbf{b} : \Omega \rightarrow \mathbb{R}^n$ is the body force. The strain tensor is given by $\boldsymbol{\varepsilon} = (\nabla \mathbf{u} + \nabla \mathbf{u}^T)/2$, where $\nabla(\cdot)$ is the gradient operator with respect to \mathbf{X} .

Here we adopt a form for ψ that accounts for the unilateral constraint following Miehe et al.³⁷ which involves spectral decomposition of $\boldsymbol{\varepsilon}$. Other choices are, for example, the volumetric-deviatoric split by Amor et al.³⁸, the micromechanics-informed model by Liu et al.³⁹, and the model by Wu et al.⁴⁰ In the chosen formulation, the strain energy density takes the following form

$$\psi(\boldsymbol{\varepsilon}, d) = g(d)\psi_+ + \psi_-, \quad (7)$$

where $g(d) = (1 - d)^2$ is the degradation function, and ψ_+ and ψ_- are, respectively, the crack-driving and persistent portions of the strain energy density as

$$\psi_{\pm}(\boldsymbol{\varepsilon}) = \frac{\lambda}{2} \langle \text{tr}(\boldsymbol{\varepsilon}) \rangle_{\pm}^2 + \mu \text{tr}(\boldsymbol{\varepsilon}_{\pm}^2), \quad (8)$$

where λ and μ are Lamé constants such that $\mu > 0$ and $\lambda + 2\mu > 0$, the Macauley bracket is defined as $\langle \cdot \rangle_{\pm} = (\cdot \pm |\cdot|)/2$, and

$$\boldsymbol{\varepsilon}_{\pm} = \sum_{a=1}^3 \langle \varepsilon_a \rangle_{\pm} \mathbf{n}_a \otimes \mathbf{n}_a, \quad (9)$$

where $\{\varepsilon_a\}_{a=1}^3$ denote the principal strains, \mathbf{n}_a are the corresponding orthonormal principal directions, and the operator \otimes represents the dyadic product. Correspondingly, the Cauchy stress tensor is

$$\boldsymbol{\sigma}_{\pm}(\boldsymbol{\varepsilon}) = \frac{\partial \psi_{\pm}}{\partial \boldsymbol{\varepsilon}} = \lambda \langle \text{tr}(\boldsymbol{\varepsilon}) \rangle_{\pm} \mathbf{1} + 2\mu \sum_{a=1}^3 \langle \varepsilon_a \rangle_{\pm} \mathbf{n}_a \otimes \mathbf{n}_a, \quad (10)$$

where $\mathbf{1}$ is the second-order identity tensor.

2.3 | Spatial discretization

In this subsection, we obtain the semi-discrete Lagrangian by discretizing the displacement field and the phase field with a finite element mesh \mathcal{T}_h for Ω . Let η be the set of nodes of \mathcal{T}_h . The discretized fields take the following form

$$\mathbf{u}(\mathbf{X}) = \sum_{a \in \eta} N_a(\mathbf{X}) \mathbf{u}_a, \quad d(\mathbf{X}) = \sum_{a \in \eta} N_a(\mathbf{X}) d_a, \quad (11)$$

where $\mathbf{u}_a \in \mathbb{R}^n$ and $d_a \in \mathbb{R}$ are the displacement vector and phase field value at node $a \in \eta$, respectively, and N_a is the finite element shape function associated with node a . In this work, quadrilateral finite elements and the associated first-order shape functions are used.

The Lagrangian L may be decomposed as

$$L(\mathbf{u}, \dot{\mathbf{u}}, d) = \sum_{e \in \mathcal{T}_h} L_e(\mathbf{u}_e, \dot{\mathbf{u}}_e, \mathbf{d}_e), \quad (12)$$

where e is an element of the mesh \mathcal{T}_h , and \mathbf{u}_e , $\dot{\mathbf{u}}_e$, and \mathbf{d}_e are the vectors containing the displacements, velocities, and phase field values of all the nodes of element e , respectively. The quantity L_e is given by

$$L_e(\mathbf{u}_e, \dot{\mathbf{u}}_e, \mathbf{d}_e) = T_e(\dot{\mathbf{u}}_e) - V_e(\mathbf{u}_e, \mathbf{d}_e) - \Gamma_e(\mathbf{d}_e), \quad (13)$$

where V_e and Γ_e are the elemental potential energy and elemental surface energy, respectively, and

$$T_e(\dot{\mathbf{u}}_e) = \frac{1}{2} \dot{\mathbf{u}}_e^T \mathbf{m}_e \dot{\mathbf{u}}_e \quad (14)$$

is the elemental kinetic energy, where \mathbf{m}_e is the diagonal element mass matrix. Hence, the space-discretized action is in the form

$$S(\{\mathbf{u}_e\}, \{\dot{\mathbf{u}}_e\}, \{\mathbf{d}_e\}) = \int_{t_0}^{t_f} \sum_{e \in \mathcal{T}_h} \left(\frac{1}{2} \dot{\mathbf{u}}_e^T \mathbf{m}_e \dot{\mathbf{u}}_e - V_e(\mathbf{u}_e, \mathbf{d}_e) - \Gamma_e(\mathbf{d}_e) \right) dt. \quad (15)$$

For later convenience, we let $\eta(e)$ denote the set of nodes of e and $\eta^{-1}(a)$ the set of elements that contain node a .

3 | ASYNCHRONOUS VARIATIONAL INTEGRATOR WITH THE FRACTURE PHASE FIELD

The main feature of the AVI is to assign different time steps to different elements of \mathcal{T}_h . The key idea is the stationarity of (15), a functional over space and time, which allows to divide the total Lagrangian into contributions from elemental terms which may possess independent time steps. For example, the smaller elements in the mesh may be updated a few times while the larger elements are held, according to either a preset schedule or a schedule determined on the fly.

In the context of fracture phase field in this work, the phase field is implicitly solved at the element level instead of at the global level, permitting more efficient solvers of inequality constraints.

In this section, we detail a phase field formulation and implementation for dynamic fracture through the AVI. The reader interested in the overall algorithmic implementation can directly go to Algorithm 2. In essence, we derive the proposed formulation from the discrete Hamilton's principle of stationary action with the fracture phase field incorporated. In addition, we adapt the reduced-space active set method to enforce the irreversibility constraint involved in the phase field problem.

3.1 | Asynchronous discretization

This subsection presents the discretization of the time domain through an asynchronous strategy. Such asynchronous discretization allows each element to have an independent time step. As an example, Figure 2 shows the spacetime diagram of a three-element mesh with asynchronous time steps.

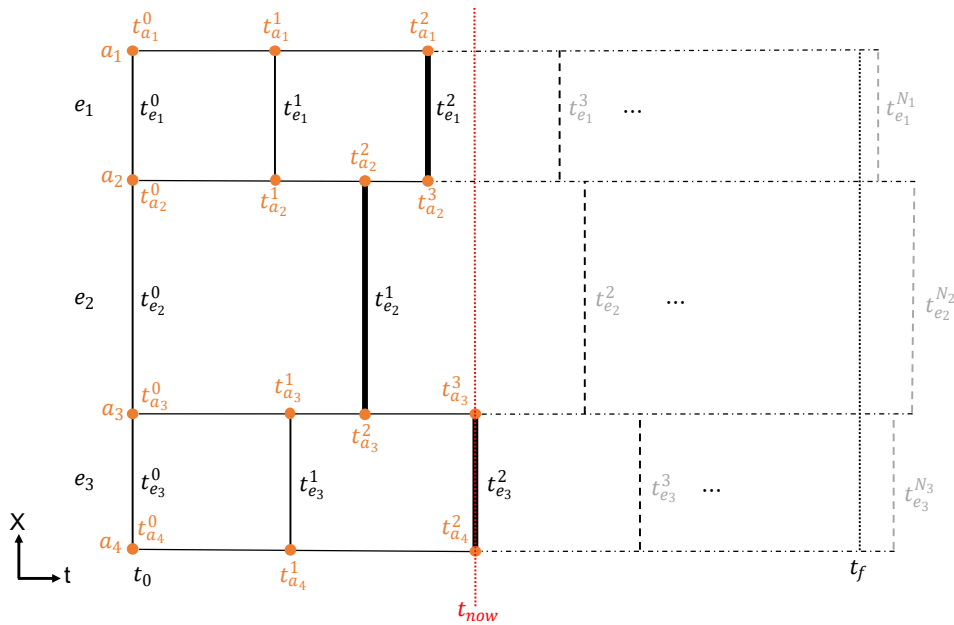


FIGURE 2 Asynchronous discretization of the time domain for a three-element mesh in the reference configuration. The entire update schedule follows the chronological order, i.e., $\Theta = \{t_{e_1}^0, t_{e_2}^0, t_{e_3}^0, t_{e_1}^1, t_{e_3}^1, t_{e_2}^1, t_{e_1}^2, t_{e_3}^2, t_{e_1}^3, t_{e_2}^3, t_{e_3}^3, \dots\}$, where $t_{now} = t_{e_3}^2$ is the current time and e_3 is the current active element.

Here, we assign to the element $e \in \mathcal{T}_h$ the update schedule

$$\Theta_e = \left\{ t_0 = t_e^0 < t_e^1 < t_e^2 \dots t_e^{N_e-1} < t_f \leq t_e^{N_e} \right\}. \quad (16)$$

At these instants, the displacements and velocities, and phase field values of all nodes $a \in \eta(e)$ are updated. In addition, we define the discrete elemental displacements $\mathbf{u}_e^j \equiv \mathbf{u}_e(t_e^j)$ and discrete elemental phase fields $\mathbf{d}_e^j \equiv \mathbf{d}_e(t_e^j)$ at $t_e^j \in \Theta_e$, and the entire

update schedule of the mesh is

$$\Theta = \bigcup_{e \in \mathcal{T}_h} \Theta_e. \quad (17)$$

For simplicity, we assume that there are no coincident instants for any pair of elements except for the initial time, i.e., $\Theta_e \cap \Theta_{e'} = \{t_0\}$ if $e \neq e'$. The general case with coincident update instants can be handled without much difficulty and will not change the results as long as elements with coincident instants are far away enough from each other.

Similarly, we also gather the schedule for node $a \in \eta$ as

$$\Theta_a = \bigcup_{e \ni a} \Theta_e = \left\{ t_0 = t_a^0 < t_a^1 < \dots < t_a^{n_a-1} < t_a^{n_a} \right\}. \quad (18)$$

We additionally define $\mathbf{u}_a^i \equiv \mathbf{u}_a(t_a^i)$, $d_a^i \equiv d_a(t_a^i)$, $t_a^i \in \Theta_a$, and the set of nodal displacements

$$\mathcal{U}_a = \left\{ \mathbf{u}_a^i : i = 0, 1, \dots, n_a \right\}, \quad a \in \eta, \quad (19)$$

and the set of nodal phase fields

$$\mathcal{D}_a = \left\{ d_a^i : i = 0, 1, \dots, n_a \right\}, \quad a \in \eta. \quad (20)$$

The triple $(\Theta, \mathcal{U}_a, \mathcal{D}_a)$ defines the discrete trajectory of the system. To solve for this triple, we write the discrete action sum as

$$S_{\text{dis}}(\Theta, \mathcal{U}_a, \mathcal{D}_a) = \sum_{e \in \mathcal{T}_h} \sum_{j=0}^{N_e-1} L_e^j, \quad (21)$$

where $L_e^j \approx \int_{t_e^j}^{t_e^{j+1}} L_e dt$.

This approximation can be realized by multiple schemes. In this paper, we adopt one such that each node $a \in \eta$ follows a linear trajectory within the time interval $[t_a^i, t_a^{i+1}]$; consequently, the corresponding nodal velocities are constant in the said interval. Moreover, the potential energy and the crack energy terms are approximated with the rectangular rule using their values at t_e^{j+1} . Then the discrete Lagrangian is

$$\int_{t_e^j}^{t_e^{j+1}} L_e dt \approx L_e^j = \sum_{a \in e} \sum_{t_a^i \in [t_e^j, t_e^{j+1}]} \frac{1}{2} \mathbf{m}_{e,a} (t_a^{i+1} - t_a^i) \left\| \frac{\mathbf{u}_a^{i+1} - \mathbf{u}_a^i}{t_a^{i+1} - t_a^i} \right\|^2 - (t_e^{j+1} - t_e^j) (V_e(\mathbf{u}_e^{j+1}, \mathbf{d}_e^{j+1}) + \Gamma_e(\mathbf{d}_e^{j+1})), \quad (22)$$

where $\mathbf{m}_{e,a}$ is the mass matrix entry of node a contributed by element e and $\mathbf{d}_e^{j+1} \equiv \mathbf{d}_e(t_e^{j+1})$ is the elemental phase field vector. Finally, the discrete action sum (21) takes the following form

$$S_{\text{dis}} = \sum_{a \in \eta} \sum_{i=0}^{n_a-1} \frac{1}{2} \mathbf{M}_a (t_a^{i+1} - t_a^i) \left\| \frac{\mathbf{u}_a^{i+1} - \mathbf{u}_a^i}{t_a^{i+1} - t_a^i} \right\|^2 - \sum_{e \in \mathcal{T}_h} \sum_{j=0}^{N_e-1} (t_e^{j+1} - t_e^j) (V_e(\mathbf{u}_e^{j+1}, \mathbf{d}_e^{j+1}) + \Gamma_e(\mathbf{d}_e^{j+1})), \quad (23)$$

where $\mathbf{M}_a = \sum_{e \in \eta^{-1}(a)} \mathbf{m}_{e,a}$.

3.2 | Discrete variational principle

In this subsection, we derive the formulation of the AVI for the phase field approach to dynamic fracture using the discrete Hamilton's principle⁴¹. Taking the partial derivative of the discrete action sum (23) with respect to \mathbf{u}_a^i follows

$$0 = \frac{\partial S_{\text{dis}}}{\partial \mathbf{u}_a^i} = \frac{\partial}{\partial \mathbf{u}_a^i} \left(\frac{1}{2} \mathbf{M}_a (t_a^i - t_a^{i-1}) \left\| \frac{\mathbf{u}_a^i - \mathbf{u}_a^{i-1}}{t_a^i - t_a^{i-1}} \right\|^2 + \frac{1}{2} \mathbf{M}_a (t_a^{i+1} - t_a^i) \left\| \frac{\mathbf{u}_a^{i+1} - \mathbf{u}_a^i}{t_a^{i+1} - t_a^i} \right\|^2 - (t_e^i - t_e^{i-1}) V_e(\mathbf{u}_e^i, \mathbf{d}_e^i) \right),$$

where $a \in \eta(e)$ such at $t_a^i = t_e^i$, which yields the discrete Euler-Lagrange equations

$$\mathbf{p}_a^{i+1/2} - \mathbf{p}_a^{i-1/2} = I_{e,a}^i = - (t_e^i - t_e^{i-1}) \frac{\partial V_e(\mathbf{u}_e^i, \mathbf{d}_e^i)}{\partial \mathbf{u}_a^i}, \quad (24)$$

where $I_{e,a}^i$ may be regarded as the impulse component of node $a \in e$ at the time $t_a^i = t_e^i$, and the discrete linear momentum is defined as

$$\mathbf{p}_a^{i-1/2} = \mathbf{M}_a \frac{\mathbf{u}_a^i - \mathbf{u}_a^{i-1}}{t_a^i - t_a^{i-1}} = \mathbf{M}_a \mathbf{v}_a^{i-1/2}. \quad (25)$$

Similarly, we take the partial derivative of (23) with respect to \mathbf{d}_e^j as follows

$$0 = \frac{\partial \mathcal{S}_{dis}}{\partial \mathbf{d}_e^j} = \frac{\partial}{\partial \mathbf{d}_e^j} [V_e(\mathbf{u}_e^j, \mathbf{d}_e^j) + \Gamma_e(\mathbf{d}_e^j)], \quad (26)$$

for element e at time t_e^j , then the phase field of element e are updated by

$$\mathbf{d}_e^j = \arg \min_{\mathbf{d}_e^* \leq \mathbf{d}_e \leq 1} \{V_e(\mathbf{u}_e^j, \mathbf{d}_e) + \Gamma_e(\mathbf{d}_e)\}, \quad (27)$$

102 where \mathbf{d}_e^* represents the phase field value of $\eta(e)$ at their most recent time of update; namely, for node $a \in \eta(e)$, at step i , \mathbf{d}_e^*
 103 contains the phase field value d_a^{i-1} . Note that normally in the same element e , \mathbf{d}_e^* may contain phase field values at different
 104 times. Here the stationarity condition (26) becomes a minimization in (27) since Γ_e is elliptic. The irreversibility constraint in (27)
 105 may be enforced in many ways, for which we have chosen the reduced-space active set strategy, to be discussed in Section 3.4.

106 Now, we consider an element $e \in \mathcal{T}_h$ with \mathbf{u}_e^{i-1} and $\mathbf{p}_a^{i-1/2}$, $a \in \eta(e)$, known at time t_e^{j-1} , also known \mathbf{d}_e^* , the provisional
 107 solution procedure is thus:

- 108 • For all $a \in \eta(e)$, solve \mathbf{u}_a^i from (25): $\mathbf{u}_a^i = \mathbf{u}_a^{i-1} + (t_a^i - t_a^{i-1})\mathbf{M}_a^{-1}\mathbf{p}_a^{i-1/2}$.
- 109 • Solve \mathbf{d}_e^j from (27).
- 110 • For all $a \in \eta(e)$, solve $\mathbf{p}_a^{i+1/2}$ from (24): $\mathbf{p}_a^{i+1/2} = \mathbf{p}_a^{i-1/2} - (t_e^j - t_e^{j-1})\partial V_e(\mathbf{u}_e^j, \mathbf{d}_e^j)/\partial \mathbf{u}_a^i$.

111 3.3 | Reformulation for solving the phase field with element patches

The solution procedure mentioned above is variational; however, the results obtained with (27) show an unreasonable crack
 pattern (see Appendix A), hence we reformulate the constrained optimization problem (27) as follows. Essentially we want to
 minimize $V + \Gamma$ with the newly obtained \mathbf{u}_e^j (same as before) while the field values of all nodes not belonging to e frozen to their
 most recent values. To this end, we define the patch for element e

$$\mathcal{T}_e = \{e' \in \mathcal{T}_h : \eta(e) \cap \eta(e') \neq \emptyset\}, \quad (28)$$

as shown in Figure 3. In this way, Eq. (27) is modified to take into account the contributions of its neighboring elements

$$\mathbf{d}_e^j = \arg \min_{\mathbf{d}_e^* \leq \mathbf{d}_e \leq 1} \sum_{e' \in \mathcal{T}_e} [V_{e'}(\{\mathbf{u}_{e'}^*, \mathbf{u}_e^j\}, \{\mathbf{d}_{e'}^*, \mathbf{d}_e\}) + \Gamma_{e'}(\{\mathbf{d}_{e'}^*, \mathbf{d}_e\})], \quad (29)$$

112 where the superscript $*$ represents the nodal values of $\eta(e') \setminus \eta(e)$ (hollow nodes in Figure 3) at their most recent time of update.

Based on the spatial discretization, the minimization problem (29) leads to the phase field residual of the element

$$\mathbf{r}_e := \int_{\mathcal{T}_e} \left[g'(d)\psi_+(\epsilon)N_a + \frac{g_c}{4c_w} \left(\frac{w'(d)N_a}{\ell} + 2\ell \nabla d \cdot \nabla N_a \right) \right] d\Omega, \quad a \in \eta(e), \quad (30)$$

where $g' = dg/dd$ and the tangent stiffness matrix of the element

$$\mathbf{k}_e := \int_{\mathcal{T}_e} \left[g''(d)\psi_+(\epsilon)N_a N_{a'} + \frac{g_c}{4c_w} \left(\frac{w''(d)N_a N_{a'}}{\ell} + 2\ell \nabla N_a \cdot \nabla N_{a'} \right) \right] d\Omega, \quad a, a' \in \eta(e). \quad (31)$$

113 For the detailed derivation of (30) and (31), the reader is referred to Shen et al.¹⁸

114 3.4 | Reduced-space active set method for irreversibility constraint

115 There are several approaches to impose the inequality constraints of the phase field when solving (29), such as the local history
 116 variable method³⁷, the penalty method⁴², and the augmented Lagrangian method⁴³.

In this work, we employ the reduced-space active set strategy⁴⁴ to ensure the phase field bounds $d \in [0, 1]$ and the
 irreversibility condition $\dot{d} > 0$. In the discrete setting, the phase field needs to satisfy the condition

$$0 \leq d_a^{i-1} \leq d_a^i \leq 1, \quad \forall i = 1, 2, \dots, n_a \text{ and } a \in \eta(e). \quad (32)$$

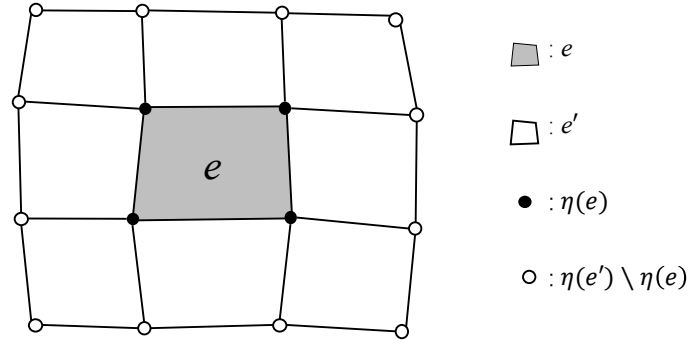


FIGURE 3 Diagram of a patch \mathcal{T}_e that consists of the element e (gray element) and its adjacent elements $e' \in \mathcal{T}_e$ (white elements). At the beginning of an iteration for element e at time t_e^j for solving the phase field \mathbf{d}_e^j , the displacements \mathbf{u}_e^j are known. Correspondingly, both the displacements $\mathbf{u}_{e'}^*$ and the phase fields $\mathbf{d}_{e'}^*$ of nodes in $\eta(e') \setminus \eta(e)$ (hollow nodes) assume their most recent values for the iteration.

Note that we solve this inequality-constrained optimization problem efficiently for only one element instead of for the entire domain. Then the solutions are determined by a mixed complementarity problem⁴⁵

$$\begin{cases} d_a^{i-1} = d_a^i, & r_a \geq 0, \\ d_a^{i-1} \leq d_a^i \leq 1, & r_a = 0, \\ d_a^i = 1, & r_a \leq 0, \end{cases} \quad (33)$$

117 where d_a^i is the nodal phase field at time $t_a^i = t_e^j$, and r_a is the phase field residual corresponding to node a . For each iteration,
118 with \mathbf{d}_e^* , \mathbf{u}_e^j , $\mathbf{d}_{e'}^*$, and $\mathbf{u}_{e'}^*$ of the patch at time t_e^j known, the phase field value of element e can be updated through Algorithm 1.

119 3.5 | Algorithmic implementation

This section focuses on the algorithmic implementation of AVI for the phase field fracture. The overall pseudo-code is provided in Algorithm 2. The time step of each element is taken as a fraction of their critical time step and is computed by

$$t_{crit} = C_{CFL} \frac{2}{\omega_e}, \quad (34)$$

120 where C_{CFL} is taken as 0.6 and ω_e is the maximum natural frequency of the element, which is the square root of the maximum
121 eigenvalue of the generalized eigenvalue problem $\mathbf{k}_e \mathbf{U} = \omega^2 \mathbf{m}_e \mathbf{U}$. The time step of each element allows certain adaptivity,
122 although we keep C_{CFL} constant in this work for simplicity.

123 Due to the asynchrony of the algorithm, we employ the priority queue⁴⁶ to keep track of the causality. The priority queue
124 assigns each element a priority according to their next update time where the element to be updated at a sooner time has a higher
125 priority. In other words, the priority queue ensures that all elements in the queue are ordered according to their next time to be
126 updated, and the top element in the queue is always the one whose next update time is the closest to the current time in the future.

127 The implementation details are shown in Algorithm 2. First, the first time steps of all elements in the mesh are computed and
128 pushed into the priority queue to establish the initial queue. Within each iteration, the priority queue pops an element (calls the
129 active element) and its next update time. The nodal displacements, phase fields, and momenta of the active element are updated
130 accordingly. Subsequently, the next update time of this element is computed and if this time is less than t_f , it is pushed into the
131 priority queue. The algorithm continues until the priority queue is empty.

132 4 | NUMERICAL EXAMPLES

133 In this section, we showcase three benchmark examples to demonstrate the ability of the proposed formulation in capturing the
134 key features of dynamic fracture. In addition, we compare the computational costs and the energy conservation behavior of our
135 approach for AT1 and AT2 models. In all examples, we use the unstructured first-order quadrilateral finite elements and refine
136 the mesh along the potential crack path.

Algorithm 1 Reduced-space active set method for solving the phase field

Input: $\mathbf{d}_e^*, \mathbf{u}_e^j, \mathbf{d}_{e'}^*, \mathbf{u}_{e'}^*, \forall e' \in \mathcal{T}_e$
Output: \mathbf{d}_e^j

- 1: Compute \mathbf{r}_e and define flag \leftarrow true
- 2: **if** $\|\mathbf{r}_e\| < \text{tol}$ **then**
- 3: flag \leftarrow false
- 4: **else**
- 5: Define $\mathcal{A} := \{a \in \eta(e) : (d_a^i = d_a^{i-1}, r_a > 0) \text{ or } (d_a^i = 1, r_a < 0)\}$ and $\mathcal{I} = \eta(e) \setminus \mathcal{A}$
- 6: **end if**
- 7: **while** flag == true **do**
- 8: Compute \mathbf{k}_e and let $\mathbf{d}_{\mathcal{A}} \leftarrow \mathbf{d}_{\mathcal{A}}^{j-1}, \mathbf{d}_{\mathcal{I}}^0 \leftarrow \mathbf{d}_{\mathcal{I}}^{j-1}$
- 9: **while** $\|\mathbf{r}_{\mathcal{I}}\| > \text{tol}$ **do**
- 10: Solve $\mathbf{d}_{\mathcal{I}}^{n+1} \leftarrow \mathbf{d}_{\mathcal{I}}^n - \mathbf{k}_{\mathcal{I}}^{-1} \mathbf{r}_{\mathcal{I}}$ and compute $\mathbf{r}_{\mathcal{I}}$, then let $n \leftarrow n + 1$
- 11: **end while**
- 12: **for** $a \in \mathcal{I}$ **do**
- 13: **if** $d_a^{n+1} > 1$ **then**
- 14: Set $d_a^{n+1} \leftarrow 1$ and $\mathcal{A} \leftarrow \mathcal{A} \cup \{a\}, \mathcal{I} \leftarrow \mathcal{I} \setminus \{a\}$
- 15: **else if** $d_a^{n+1} < d_a^n$ **then**
- 16: Set $d_a^{n+1} \leftarrow d_a^n$ and $\mathcal{A} \leftarrow \mathcal{A} \cup \{a\}, \mathcal{I} \leftarrow \mathcal{I} \setminus \{a\}$
- 17: **end if**
- 18: **end for**
- 19: Compute $\mathbf{r}_{\mathcal{A}}$ from (30)
- 20: **if** $\forall a \in \mathcal{A}$ satisfy Eq. (33) **then**
- 21: flag \leftarrow false
- 22: **else**
- 23: For each $a \in \mathcal{A}$ not satisfying Eq. (33), $\mathcal{I} \leftarrow \mathcal{I} \cup \{a\}$
- 24: **end if**
- 25: **end while**

TABLE 1 Material properties for the numerical examples in Section 4.

Parameter	Symbol	Section 4.1	Section 4.2	Section 4.3
Material	-	Silica glass	Soda-lime glass	Maraging steel 18Ni(300)
Young's modulus (GPa)	E	32	72	190
Poisson's ratio	ν	0.2	0.22	0.3
Density (kg/m ³)	ρ	2450	2440	8000
Critical energy release rate (J/m ²)	g_c	3	3.8	2.213×10^4
Rayleigh speed (m/s)	v_R	2119	3172	2803

137 A note on the post-processing is as follows. We sample the solution at a frequency of every 500,000 elemental iterations.
138 For example, if the current time $t_{now} = t_{e_3}^2$ in Figure 2 happens to be a sampling time, then post-processing results are obtained
139 using the most recent nodal displacement, velocity, and phase field values prior to t_{now} , i.e., values at nodal times $t_{a_1}^2, t_{a_2}^3, t_{a_3}^3, t_{a_4}^2$
140 for the nodes shown. For example, the crack patterns to be plotted are obtained using the most recent phase field values prior to
141 the sampling times. More accurate results can be obtained by interpolation using the values before and after the sampling time,
142 which is not undertaken in this work for simplicity.

Algorithm 2 Algorithm of AVI for the phase field to fracture

Input: $\mathcal{T}_h, \eta, \Theta, Q = \emptyset$ and $\{\mathbf{u}_a^0, \mathbf{d}_e^0, \mathbf{p}_a^{1/2} \mid a \in \eta\}$
Output: $\mathbf{u}_a^i, \mathbf{d}_e^j, \mathbf{p}_a^{i+1/2}$, where $i, j = 1, 2, 3, \dots$, corresponding to Θ

- 1: Initialization: $\mathbf{u}_a \leftarrow \mathbf{u}_a^0, \mathbf{d}_e \leftarrow \mathbf{d}_e^0, \mathbf{p}_a \leftarrow \mathbf{p}_a^{1/2}, \tau_a \leftarrow t_0$ for all $a \in \eta$
- 2: **for all** $e \in \mathcal{T}_h$ **do**
- 3: $\tau_e \leftarrow t_0$
- 4: Compute t_e^1 and push (t_e^1, e) into priority queue Q
- 5: **end for**
- 6: **while** Q is not empty **do**
- 7: Extract next element: pop (t, e) from Q
- 8: Compute displacements \mathbf{u}_e with (25) and update node's time $\tau_a \leftarrow t$ for all $a \in \eta(e)$
- 9: Compute the phase fields \mathbf{d}_e with (29) following Algorithm 1
- 10: **if** $t < t_f$ **then**
- 11: Compute momentum \mathbf{p}_a with (24) for all $a \in \eta(e)$
- 12: Update element's time: $\tau_e \leftarrow t$
- 13: Compute t_e^{next} and schedule e for next iterate: push (t_e^{next}, e) into Q
- 14: **end if**
- 15: **end while**

4.1 | Boundary tension test

In this section, a pre-notched rectangular plate loaded dynamically in tension is modeled. The geometry and boundary conditions are shown in Figure 4. A constant traction $\sigma^* = 1$ MPa is applied on the top and bottom edges throughout the simulation and the remaining boundary is traction free. This benchmark problem has been widely studied, for example by Song et al.⁴⁷ using the extended finite element method, by Nguyen⁷ with the cohesive zone method, and by Borden et al.¹⁹ with a synchronous phase field approach to fracture, as well as in experimental studies^{48,49}. As described in Ref. 48, a crack emerges at the notch tip and starts propagating to the right in a stable way. Over a certain distance, the main crack branches into two symmetrical sub-cracks and continue growing until it reaches the right surface.

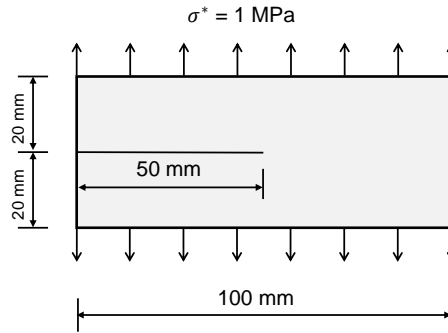


FIGURE 4 Geometry and boundary conditions of the boundary tension test, in which a pre-notched plate is under tension.

The material used in this test is silica glass and its properties are listed in Table 1. A plain strain state with a unit thickness is assumed. The length scale parameter takes $\ell = 5 \times 10^{-4}$ m, which is small enough with respect to the specimen dimensions. Two different mesh levels are used: Mesh 1 with $h = 2.5 \times 10^{-4}$ m = $\ell/2$, and Mesh 2 with $h = 1.25 \times 10^{-4}$ m = $\ell/4$.

The final phase field results are shown in Figure 5. As seen, there is no significant difference of the crack pattern between the AT2 and AT1 models. The crack branches at between 34 and 36 μ s and reaches the right boundary at $t \approx 80 \mu$ s. The upper crack branching angle is around 27.5°, which agrees well with the results in Refs. 50,20. In addition, the bifurcation angle of

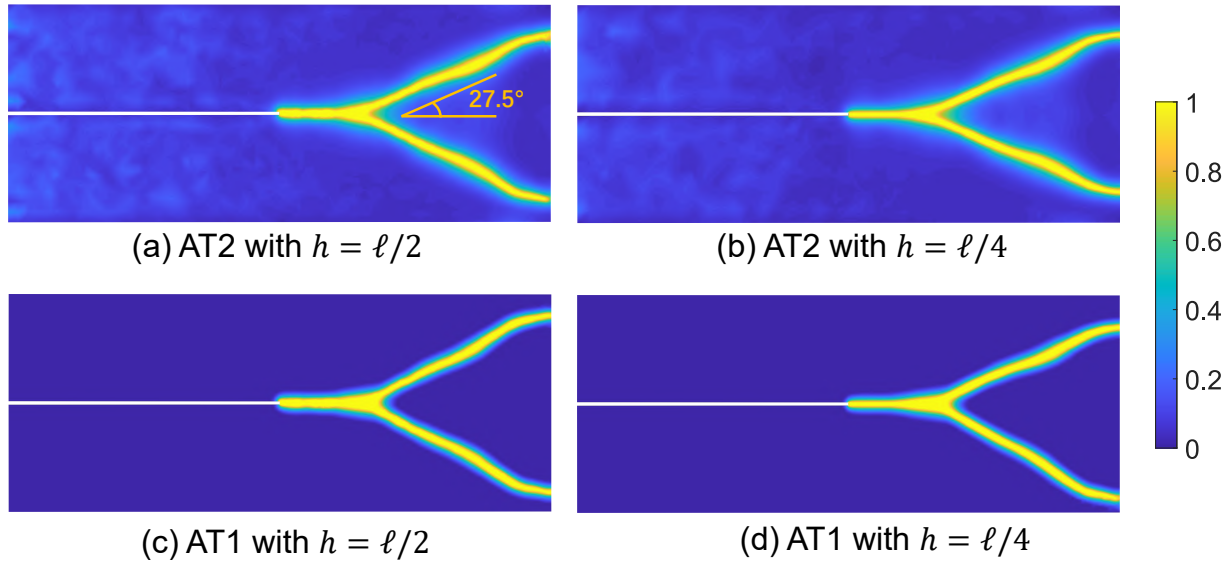


FIGURE 5 Phase field results for the boundary tension test of AT1/2 models.

157 the lower branch is slightly different from that of the upper one, which may be caused by the non-symmetric discretization of
 158 the mesh. This non-perfect symmetry was also observed by Ren et al.³⁵

Figure 6(a) shows the evolution of the total crack tip velocity calculated by

$$v_{tip} = \frac{1}{g_c} \frac{d\Gamma}{dt}, \quad (35)$$

159 and normalized by the Rayleigh wave speed. In particular, the derivative is obtained by comparing the values of Γ at consecutive
 160 sampling times. It is observed that at the beginning, a single main crack propagates to the right with a speed less than 60% of
 161 the Rayleigh wave speed. Then, the main crack branches into two sub-cracks and in this respect the total crack tip velocity of
 162 both branches is plotted, which is still less than 60% of twice the Rayleigh wave speed. Therefore, whether before or after the
 163 branching emerges, the velocity is in a reasonable range. Moreover, the overall propagation speed during the evolution is in good
 164 agreement with the results reported in a numerical study¹³ and an experimental study⁴⁸.

165 Figure 6 (b)-(d) present the evolution of the crack surface energy, strain energy, and kinetic energy, respectively. The crack
 166 surface energy monotonically increases as expected due to the unilaterality of the phase field. In addition, the strain energy
 167 evidently shows the periodic oscillation at the beginning and this trend gradually weakens with crack evolution, because the
 168 stress wave is reflected at the boundaries and cracks, and interacts with itself.

169 Figure 6(e) shows the evolution of the external work, which is calculated from the second term on the right hand side of
 170 Eq. (6). It is clear that the kinetic energy accounts for most of the energy converted from external work.

171 Figure 6(f) shows the evolutions of the free energy $T(\dot{\mathbf{u}}) + V(\mathbf{u}, d) + \Gamma(d)$. The free energy is negative and its magnitude is
 172 only 1.32% of the external work at the end. This small negative numbers demonstrate that the method possesses remarkable
 173 energy conservation property and is energetically stable.

174 Figure 7 shows the maximum principal stress with Mesh 1 at $t = 70 \mu\text{s}$. Therein, stress concentration is clearly seen at the
 175 crack tips and the results are in good agreement with those in Ref. 51.

176 Table 2 collects some statistics of the computational cost for the example at hand. As a platform-independent indicator, the
 177 number of updates of each element throughout the simulation for each case is counted. The second, third, and fourth columns
 178 represent the minimum, maximum, and median numbers of updates among the elements, respectively. The fifth column is the
 179 total numbers of updates of all elements of AVI. The sixth column is the total numbers of updates of synchronous integration,
 180 where the data is estimated by assuming the global critical time step is used for the same time interval $[t_0, t_f]$. As shown, the
 181 total numbers of AVI updates is approximately 31% of those of synchronous integration. Considering that it is even more costly
 182 to implicitly solve for the phase field with a synchronous method per time step, the data in Table 2 indicates that the proposed
 183 scheme effectively reduces the computational cost compared with synchronous methods.

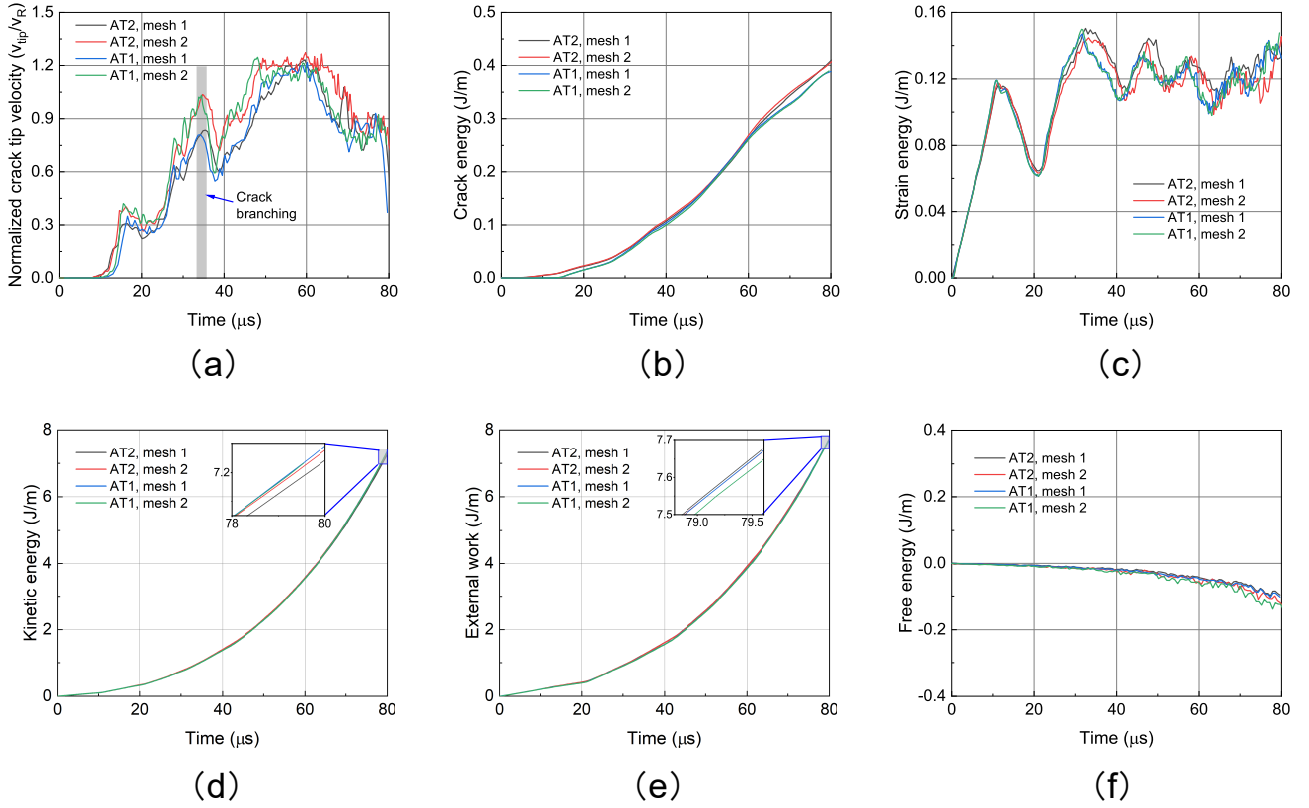


FIGURE 6 Results of the boundary tension test. Evolution of (a) normalized total crack tip velocity; (b) crack energy $\Gamma(d)$; (c) strain energy; (d) kinetic energy $T(\dot{\mathbf{u}})$; (e) external work; (f) free energy $T(\dot{\mathbf{u}}) + V(\mathbf{u}, d) + \Gamma(d)$. Here for (e) as well as for (b)(c)(d) the results are obtained by sampling. It can be seen that the free energy is 1.32% of the external work at the end, indicating the conservation of energy.

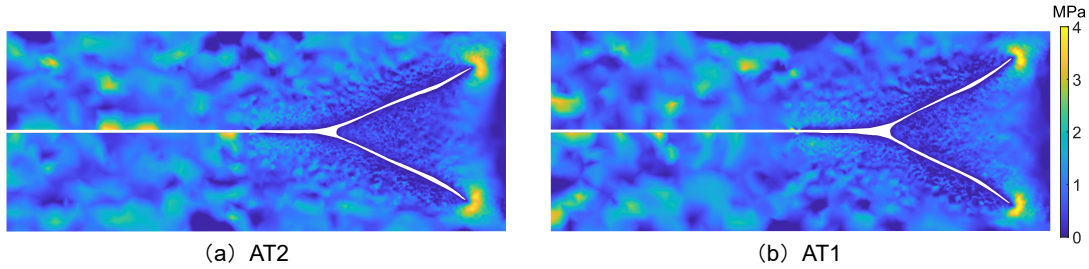


FIGURE 7 Boundary tension test: maximum principal stress with Mesh 1 at $t = 70 \mu s$, where $d > 0.9$ are removed.

TABLE 2 Numbers of elemental updates for the boundary tension test during the entire simulation.

Mesh & Model	Min.	Max.	Median	AVI total [†]	Synchronous integration (estimated) [‡]
Mesh 1, AT2	178	5,983	2,106	27,400,002	86,382,554
Mesh 1, AT1	178	5,983	2,106	27,400,002	86,382,554
Mesh 2, AT2	160	10,150	3,440	62,285,189	201,051,200
Mesh 2, AT1	160	10,150	3,440	62,285,189	201,051,200

[†]Total numbers of the elements involved in the update of the mechanical field and phase field.

[‡]This column of data is estimated by assuming the global critical time step is used throughout the computation for the same desired time interval $[t_0, t_f]$.

4.2 | Compact tension test

In this section, we investigate a series of dynamic loads applied on pre-crack surfaces as the compact tension (CT) test. The geometry and boundary conditions are shown in Figure 8. Three different constant normal tractions $\sigma^* = \{0.5, 3, 6\}$ MPa are applied on the pre-crack surfaces. This benchmark problem has been studied by Bobaru and Zhang⁵² using peridynamics and Mandal et al.⁵³ with a synchronous phase field approach.

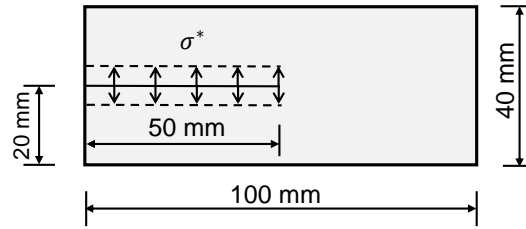


FIGURE 8 Geometry and boundary conditions for the dynamic CT test.

The material is assumed to be soda-lime glass, whose properties are given in Table 1. Plain strain state is assumed. The length scale parameter $\ell = 5 \times 10^{-4}$ m and the mesh size $h = 2.5 \times 10^{-4}$ m = $\ell/2$ are used for all cases. Figure 9 shows the phase field results for the CT test. For $\sigma^* = 0.5$ MPa a straight crack without branching is obtained. For larger values of σ^* crack branching is observed and the branching location moves to the left with the increase of σ^* . The crack branching happens at around 17.3 μ s and 9.2 μ s, and the branching angles are 52° and 46° for $\sigma^* = 3$ MPa and 6 MPa, respectively. Also, there is no significant difference of the crack patterns between the AT2 and AT1 models for the same load. Moreover, the crack patterns, branching instants, and branching angles are all in good agreement with the results reported in Ref. 53.

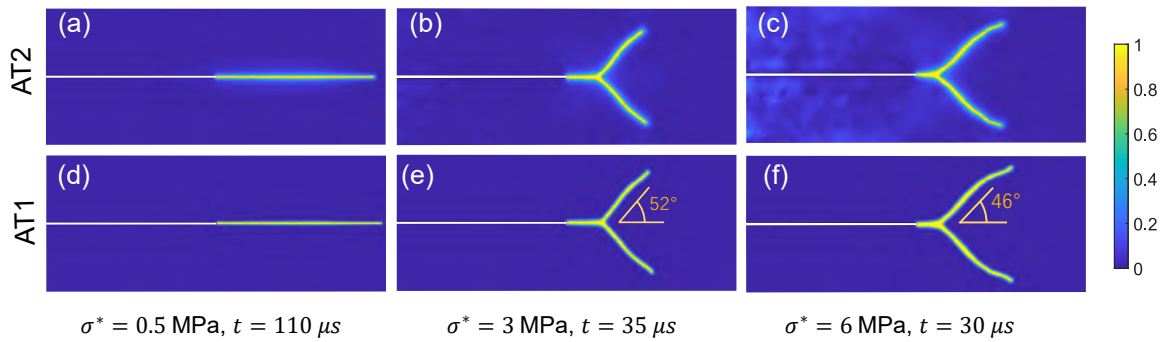


FIGURE 9 Phase field results for the CT test of AT1/2 models under different loads.

Figure 10(a) illustrates the normalized total crack tip velocity of CT test for $\sigma^* = 3$ MPa. Like the case of Figure 6(a), a main crack propagates to the right with an increasing speed less than 60% of the Rayleigh wave speed. Then, then main crack branches into two sub-cracks and the total speed is still less than 60% of twice the Rayleigh wave speed. Figure 10(b) shows the crack energy. Figure 10(c) shows the evolution of the strain energy. An interesting observation is that the curve presents a periodic oscillation with a period of approximately 6.8 μ s, which can be explained as follows. During the process, the stress waves propagate from the crack to the top and bottom boundaries and then are reflected until they meet the crack again. The time it takes the stress wave to travel a round trip can be estimated by $l/v_D = 6.89$ μ s, where $l = 40$ mm is twice the half-width of the specimen and $v_D = 5800$ m/s is the dilatational wave speed of soda-lime glass. This process is repeated, and hence the periodicity. Figure 10(d-e) show the kinetic energy and external work, both of which monotonically increase. Figure 10(f) shows the free energy of the AT2 and AT1 model during the evolution. As we can see, the magnitude of the free energy only accounts for 1.69% of the external work, which indicates the conservation of energy.

Figure 11 shows the maximum principal stress for $\sigma^* = 3$ MPa and 6 MPa, respectively.

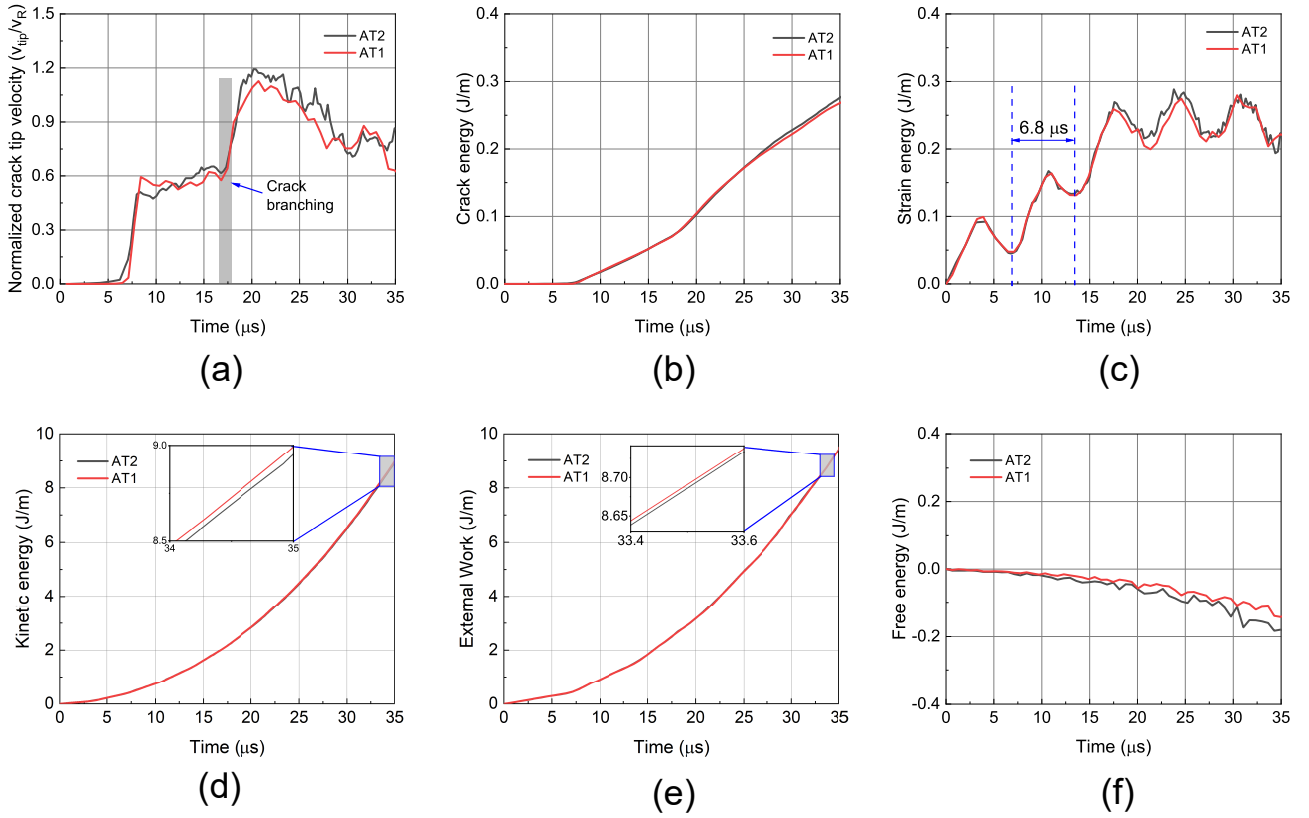


FIGURE 10 Results of the CT test for $\sigma^* = 3$ MPa. Evolution of: (a) normalized total crack propagation velocity; (b) crack energy; (c) strain energy; (d) kinetic energy; (e) external work; (f) free energy. The free energy is only 1.69% of the external work, which indicates the conservation of energy.

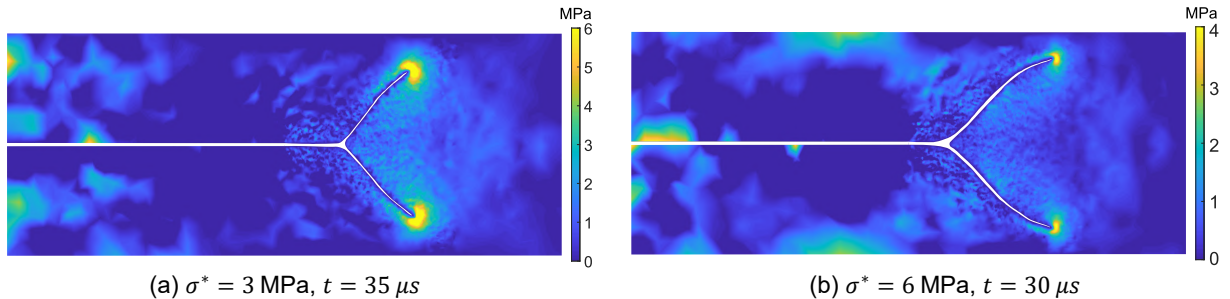


FIGURE 11 Maximum principal stress from the CT test for the AT1 model.

4.3 | The Kalthoff-Winkler test

This section studies the Kalthoff-Winkler experiment in which an edge-cracked plate is under impact velocity. Due to symmetry, only half of the plate is considered. The geometry and boundary conditions are shown in Figure 12. In the experiment^{54,55}, the brittle failure mode with a crack propagating at about 70° was observed at a certain impact speed, and the relevant numerical results were reported by other researchers using the extended finite element method⁴⁷, peridynamics⁵⁶, and the gradient damage method¹¹.

The material is maraging steel 18Ni(300), whose properties are given in Table 1. A plane strain state is assumed. The length scale parameter $\ell = 3.9 \times 10^{-4}$ m and two different meshes are used: Mesh 1 with size $h = 1.95 \times 10^{-4}$ m = $\ell/2$ and Mesh 2 with $h = 9.75 \times 10^{-5}$ m = $\ell/4$.

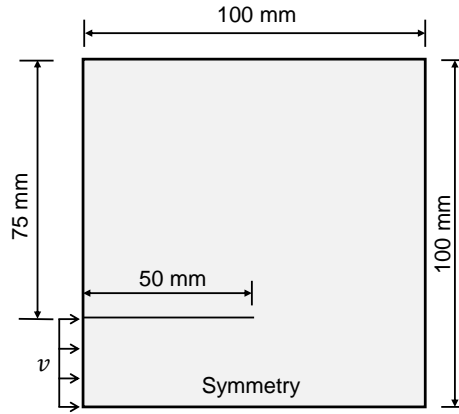


FIGURE 12 Geometry and boundary conditions of the Kalthoff test, where $v = 16.5$ m/s.

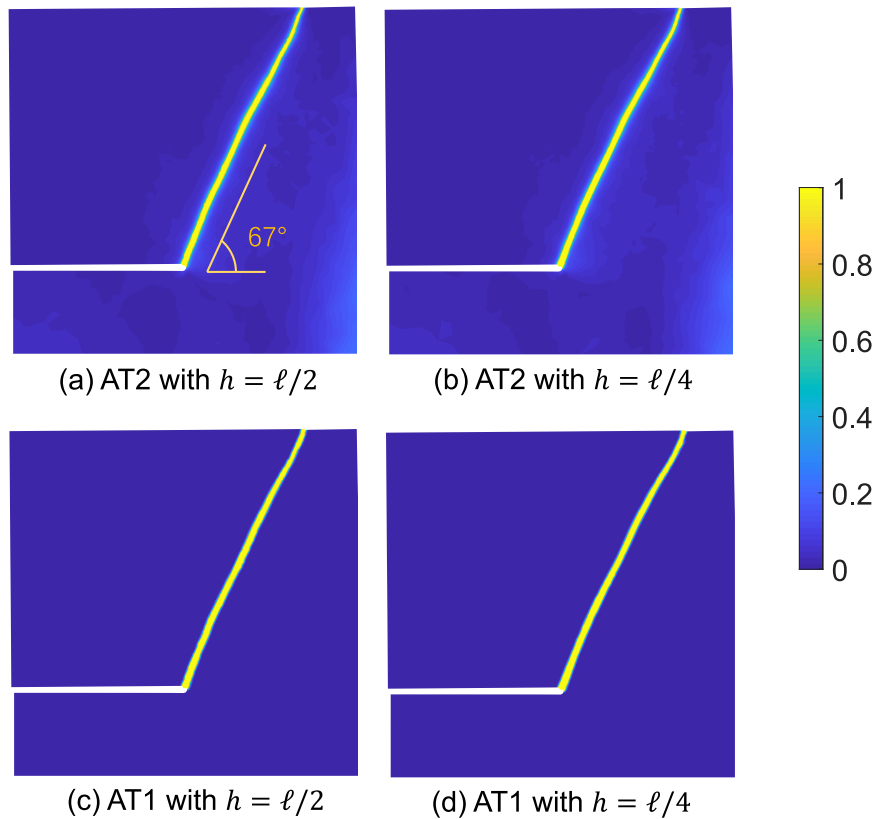


FIGURE 13 Phase field results for the Kalthoff test of AT1/2 models at time $t = 87 \mu\text{s}$.

217 Figure 13 shows the final phase field patterns at $t = 87 \mu\text{s}$ for different meshes and models. The crack propagates at $25.5 \mu\text{s}$
 218 and with an angle of about 67° with the horizontal line, which is in good agreement with the experimental results⁵⁴ and the
 219 numerical results using the phase field method^{57,58}.

220 Figure 14(a) presents the normalized crack tip velocity of the Kalthoff test, the velocity is almost two times the result reported
 221 by Liu et al.⁵¹ The differences in crack tip velocity may be caused by the different post-processing methods, where Ref. 51
 222 employed an alternative method that is different from ours by Eq. (35), to be discussed later. Figure 14(b) shows the crack energy
 223 calculated by (4), which agrees well with the numerical results in Ref. 43. In addition, the crack energy of the AT2 model is
 224 a little higher than the AT1 model for both meshes. Figure 14(c) and (d) show the evolution of the strain energy and kinetic
 225 energy, respectively, and the results are consistent with numerical results reported by Zhang et al.⁵⁹ Figure 14(e) shows the

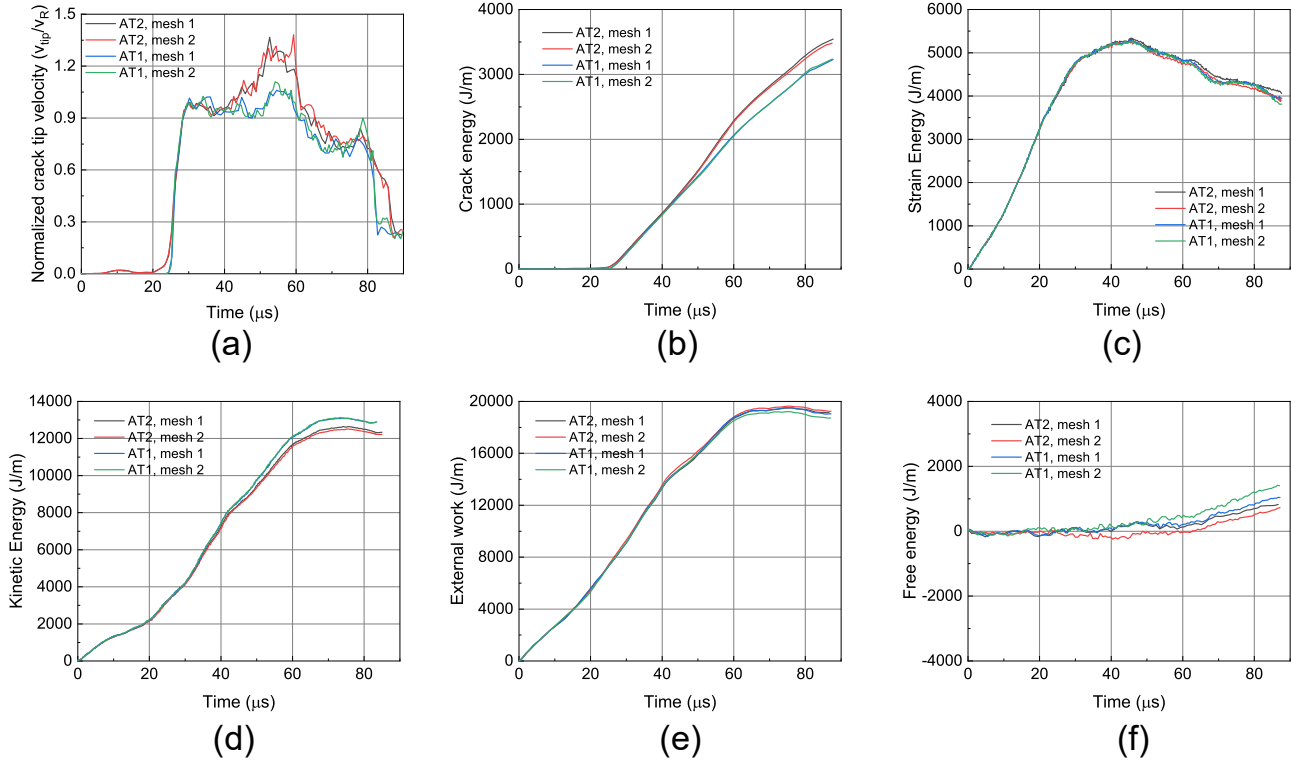


FIGURE 14 Results of the Kalthoff test. Evolution of (a) normalized crack tip velocity; (b) crack energy; (c) strain energy; (d) kinetic energy; (e) external work; (f) free energy. The external work (e) is obtained by sampling the power of the reaction force, and then integrating this power with respect to time. The free energy gradually increases, reaching between 3.74% and 7.34% of the external work in the end, which seems to violate the law of conservation of energy. See Figure 16 for a comparison.

226 external work, to the best of our knowledge, there is no relevant report on external work of the Kalthoff test by the phase field
 227 method at present. However, our result is in good agreement with the result using the cohesive zone model by Park et al.⁶⁰ Figure
 228 14(f) shows the evolution of the free energy. As we can see, the free energy gradually increases, reaching between 715.34 J and
 229 1403.51 J at the end of the simulation, which seems to violate the law of conservation of energy. This phenomenon appears to
 230 be an open question.

231 Figure 15 shows the distribution of the maximum principal stress for Mesh 2. The stress concentration is clearly seen at the
 232 crack tip, also the bottom right corner, in both AT2 and AT1 models. The result is in good agreement with those in Liu et al.⁵¹

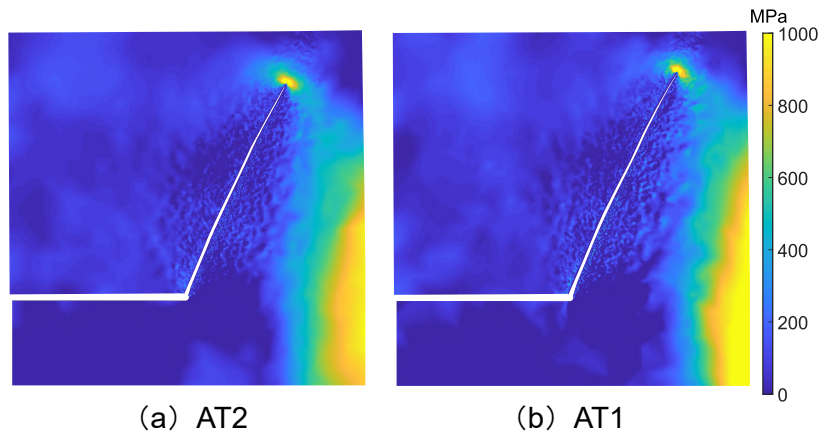


FIGURE 15 Maximum principal stress of Kalthoff test for Mesh 2 at $t = 70 \mu s$.

Alternative method to calculate the crack tip velocity

As an attempt to reconcile the discrepancy, we employ the iso-curve strategy to calculate the crack tip velocity, as also done by Liu et al.⁵¹ In this approach, the position of the crack tip is determined by the iso-curve with phase field $d = 0.9$. Therefore, the crack tip velocity is recalculated by $v_n = \|\mathbf{x}_n - \mathbf{x}_{n-1}\|/(t_n - t_{n-1})$, where \mathbf{x}_n represents the location of the crack tip at n th sampling time t_n , and the result is shown in Figure 16(a). As can be seen, the crack accelerates to near $0.6v_R$ and then remains with this velocity during the propagation until it reaches the top boundary, which agrees well with the result reported in Ref. 51.

With this iso-curve scheme, the four cases of Kalthoff test show a similar final crack length of approximately $l_{crack} = 83$ mm, see Figure 16(b) with the right vertical axis. Correspondingly, the crack energy can be computed as

$$\hat{\Gamma} = g_c l_{crack}, \quad (36)$$

with the value of 1836.79 J for a sharp crack, see Figure 16(b) with the left vertical axis. A significant difference is that $\hat{\Gamma}$ is much smaller than Γ , and the ratios of $\Gamma/\hat{\Gamma}$ are 1.9 and 1.75 for the AT2 and AT1 models, respectively.

In addition, we recalculate the free energy by using (36) instead of (4), i.e., $T(\dot{\mathbf{u}}) + V(\mathbf{u}, d) + \hat{\Gamma}$, and the result is shown in Figure 16(c). As seen, with $\hat{\Gamma}$, the results are energetically stable and satisfy the conservation of energy.

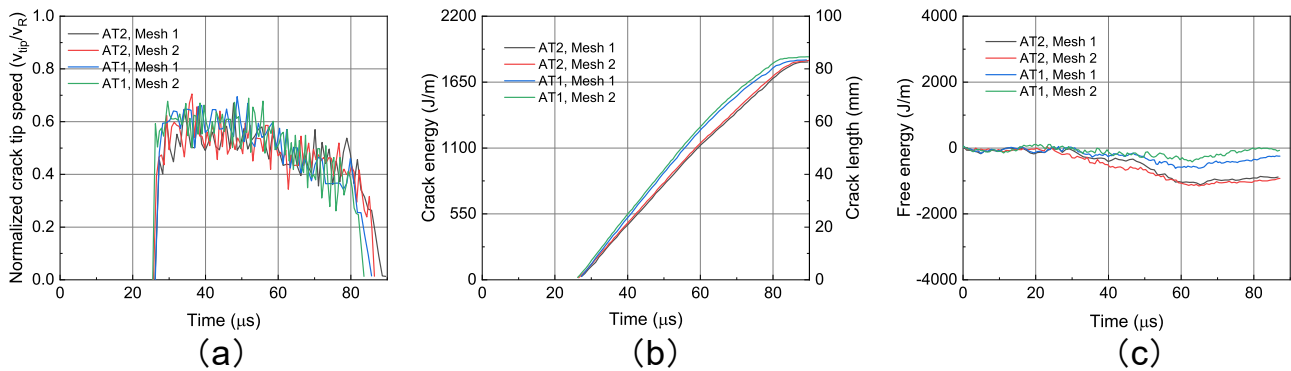


FIGURE 16 Results of the Kalthoff test. Evolution of (a) normalized crack tip velocity calculated by iso-curve strategy; (b) crack energy calculated by Eq. (36), i.e., $\hat{\Gamma}$ (left vertical axis), and crack length (right vertical axis); (c) free energy $T(\dot{\mathbf{u}}) + V(\mathbf{u}, d) + \hat{\Gamma}(d)$, which satisfies the conservation of energy.

Discussions

In the Kalthoff test, the crack energy calculated by (4) is higher than that by (36). This phenomenon is not unique to this work but also reported in Refs. 19,51,58,43,59,61,62, in which the ratio of $\Gamma/\hat{\Gamma}$ is between 1.90 and 2.45, equal to or even higher than our value. Meanwhile, in Ref. 20, this ratio is 1.37. In addition, this phenomenon was also reported in other dynamic phase field fracture by Ziaei-Rad and Shen²⁴, where the ratio is approximately 2.

Although the main reason why Γ is higher than $\hat{\Gamma}$ need to be further investigated, we suggest that the way of enforcing irreversibility constraint is not an ideal candidate. Borden et al.¹⁹ suggested that the strain-history field (alternative way to enforce the irreversibility) could play an important role, but the ratio of $\Gamma/\hat{\Gamma}$ is still 1.4 despite the strain-history field being removed which allows the crack to heal. In addition, Geelen et al.⁴³ employed the augmented Lagrangian method to enforce the irreversibility and the resulting ratio is 2.

Moreover, Li et al.¹¹ stated that the numerical phase field of the Kalthoff test is wider than the analytical one, and the wider damage profile will lead to an amplified effective fracture toughness, which had also been reported by Bourdin et al.⁶³ Furthermore, Bleyer et al.⁶⁴ suggested that the mesh size has an influence on the result of both quasi-static and dynamic fracture and that will further lead to an overestimated crack energy (see Eqs. (16) and (17) in Ref. 64 for more details).

This issue appears to be an open question for the Kalthoff test.

5 | CONCLUSIONS

In this paper, we have proposed an asynchronous variational formulation for the phase field approach to dynamic brittle fracture. The formulation is derived from Hamilton's principle of stationary action and to a great extent, retains the advantages of variational integrators. A major characteristic of the formulation is that it allows elements to have independent time steps. The result indicates that the formulation is able to simulate the dynamic fracture propagation and branching successfully. As a result of the variational structure, the formulation performs a remarkable energy behavior during the simulation. Compared to synchronous methods, the presented formulation improves the computational efficiency for problems involving a high contrast in element sizes or material properties.

Another characteristic is that the phase field irreversibility condition is enforced by the reduced-space active set method at the level of element patches. As a result, AT2 and AT1 variants of the phase field approach may be implemented with similar costs. The present study shows that these two variants lead to similar results at roughly the same computational cost.

ACKNOWLEDGMENTS

We acknowledge the financial support by the National Natural Science Foundation of China, Grant No. 11972227, and by the Natural Science Foundation of Shanghai, Grant No. 19ZR1424200.



APPENDIX

A PHASE FIELD RESULT WITHOUT USING ELEMENT PATCHES

Figure A1 shows the phase field result obtained with (27), i.e., without patches, the boundary conditions and material properties are the same as those of Section 4.1. As seen, the crack patterns are too diffused.

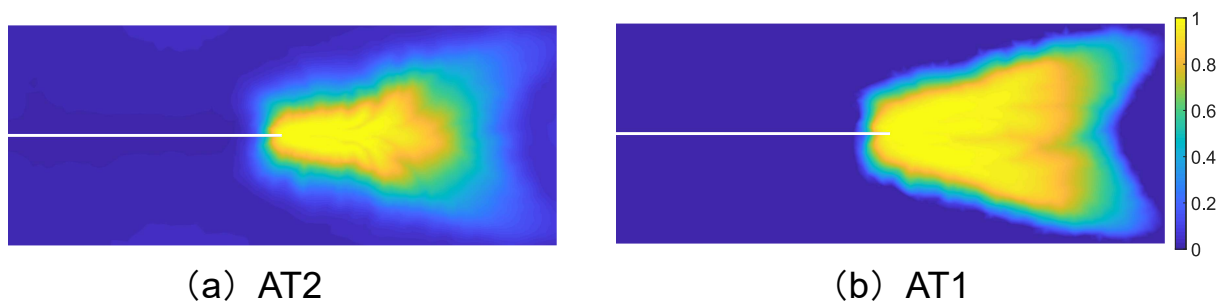


FIGURE A1 Phase field result with the formulation without using patches.

References

1. Freund LB. *Dynamic Fracture Mechanics*. Cambridge University Press . 1998.
2. Ravi-Chandar K. *Dynamic Fracture*. Elsevier . 2004.
3. Fineberg J, Bouchbinder E. Recent developments in dynamic fracture: Some perspectives. *International Journal of Fracture* 2015; 196(1-2): 33–57. doi: <https://doi.org/10.1007/s10704-015-0038-x>

- 282 4. Sun Y, Edwards MG, Chen B, Li C. A state-of-the-art review of crack branching. *Engineering Fracture Mechanics* 2021;
283 257: 108036. doi: <https://doi.org/10.1016/j.engfracmech.2021.108036>
- 284 5. Rabczuk T. Computational methods for fracture in brittle and quasi-brittle solids: State-of-the-art review and future
285 perspectives. *International Scholarly Research Notices* 2013; 2013: 1-38. doi: <https://doi.org/10.1155/2013/849231>
- 286 6. Réthoré J, Gravouil A, Combescure A. An energy-conserving scheme for dynamic crack growth using the eXtended
287 finite element method. *International Journal for Numerical Methods in Engineering* 2005; 63(5): 631-659. doi:
288 <https://doi.org/10.1002/nme.1283>
- 289 7. Nguyen VP. Discontinuous Galerkin/extrinsic cohesive zone modeling: Implementation caveats and appli-
290 cations in computational fracture mechanics. *Engineering Fracture Mechanics* 2014; 128: 37-68. doi:
291 <https://doi.org/10.1016/j.engfracmech.2014.07.003>
- 292 8. Liu Y, Filonova V, Hu N, et al. A regularized phenomenological multiscale damage model. *International Journal for*
293 *Numerical Methods in Engineering* 2014; 99(12): 867-887. doi: <https://doi.org/10.1002/nme.4705>
- 294 9. Zhang Y, Zhuang X. Cracking elements method for dynamic brittle fracture. *Theoretical and Applied Fracture Mechanics*
295 2019; 102: 1-9. doi: <https://doi.org/10.1016/j.tafmec.2018.09.015>
- 296 10. Song JH, Areias PMA, Belytschko T. A method for dynamic crack and shear band propagation with phantom nodes.
297 *International Journal for Numerical Methods in Engineering* 2006; 67(6): 868-893. doi: <https://doi.org/10.1002/nme.1652>
- 298 11. Li T, Marigo JJ, Guilbaud D, Potapov S. Gradient damage modeling of brittle fracture in an explicit dynamics context. *Inter-*
299 *national Journal for Numerical Methods in Engineering* 2016; 108(11): 1381-1405. doi: <https://doi.org/10.1002/nme.5262>
- 300 12. Moreau K, Moës N, Picart D, Stainier L. Explicit dynamics with a non-local damage model using the thick
301 level set approach. *International Journal for Numerical Methods in Engineering* 2015; 102(3-4): 808-838. doi:
302 <https://doi.org/10.1002/nme.4824>
- 303 13. Bourdin B, Francfort G, Marigo JJ. Numerical experiments in revisited brittle fracture. *Journal of the Mechanics and Physics*
304 *of Solids* 2000; 48(4): 797-826. doi: [https://doi.org/10.1016/S0022-5096\(99\)00028-9](https://doi.org/10.1016/S0022-5096(99)00028-9)
- 305 14. Francfort G, Marigo JJ. Revisiting brittle fracture as an energy minimization problem. *Journal of the Mechanics and Physics*
306 *of Solids* 1998; 46(8): 1319-1342. doi: [https://doi.org/10.1016/S0022-5096\(98\)00034-9](https://doi.org/10.1016/S0022-5096(98)00034-9)
- 307 15. Amiri F, Millán D, Shen Y, Rabczuk T, Arroyo M. Phase-field modeling of fracture in linear thin shells. *Theoretical and*
308 *Applied Fracture Mechanics* 2014; 69: 102-109. doi: <https://doi.org/10.1016/j.tafmec.2013.12.002>
- 309 16. Lai W, Gao J, Li Y, Arroyo M, Shen Y. Phase field modeling of brittle fracture in an Euler–Bernoulli beam accounting
310 for transverse part-through cracks. *Computer Methods in Applied Mechanics and Engineering* 2020; 361: 112787. doi:
311 <https://doi.org/10.1016/j.cma.2019.112787>
- 312 17. Mollaali M, Ziaei-Rad V, Shen Y. Numerical modeling of CO2 fracturing by the phase field approach. *Journal of Natural*
313 *Gas Science and Engineering* 2019; 70: 102905. doi: <https://doi.org/10.1016/j.jngse.2019.102905>
- 314 18. Shen Y, Mollaali M, Li Y, Ma W, Jiang J. Implementation details for the phase field approaches to fracture. *Journal of*
315 *Shanghai Jiaotong University (Science)* 2018; 23(1): 166–174. doi: <https://doi.org/10.1007/s12204-018-1922-0>
- 316 19. Borden MJ, Verhoosel CV, Scott MA, Hughes TJ, Landis CM. A phase-field description of dynamic brittle
317 fracture. *Computer Methods in Applied Mechanics and Engineering* 2012; 217-220: 77-95. doi:
318 <https://doi.org/10.1016/j.cma.2012.01.008>
- 319 20. Nguyen VP, Wu JY. Modeling dynamic fracture of solids with a phase-field regularized cohesive zone model. *Computer*
320 *Methods in Applied Mechanics and Engineering* 2018; 340: 1000-1022. doi: <https://doi.org/10.1016/j.cma.2018.06.015>
- 321 21. Hao S, Shen Y, Cheng JB. Phase field formulation for the fracture of a metal under impact with a fluid formulation.
322 *Engineering Fracture Mechanics* 2022; 261: 108142. doi: <https://doi.org/10.1016/j.engfracmech.2021.108142>

- 323 22. Hao S, Chen Y, Cheng JB, Shen Y. A phase field model for high-speed impact based on the updated Lagrangian formulation.
324 *Finite Elements in Analysis and Design* 2022; 199: 103652. doi: <https://doi.org/10.1016/j.finel.2021.103652>
- 325 23. Tian F, Tang X, Xu T, Yang J, Li L. A hybrid adaptive finite element phase-field method for quasi-static and
326 dynamic brittle fracture. *International Journal for Numerical Methods in Engineering* 2019; 120(9): 1108-1125. doi:
327 <https://doi.org/10.1002/nme.6172>
- 328 24. Ziaei-Rad V, Shen Y. Massive parallelization of the phase field formulation for crack propagation with time adaptivity. *Com-*
329 *puter Methods in Applied Mechanics and Engineering* 2016; 312: 224-253. doi: <https://doi.org/10.1016/j.cma.2016.04.013>
- 330 25. Li Y, Lai W, Shen Y. Variational h-adaption method for the phase field approach to fracture. *International Journal of*
331 *Fracture* 2019; 217: 83-103. doi: <https://doi.org/10.1007/s10704-019-00372-y>
- 332 26. Engwer C, Pop IS, Wick T. Dynamic and weighted stabilizations of the L-scheme applied to a phase-field model for fracture
333 propagation. In: Springer International Publishing; 2021; Cham: 1177–1184
- 334 27. Lew A, Marsden JE, Ortiz M, West M. Asynchronous variational integrators. *Archive for Rational Mechanics and Analysis*
335 2003; 167(2): 85–146. doi: <https://doi.org/10.1007/s00205-002-0212-y>
- 336 28. Lew A, Marsden J, Ortiz M, West M. Variational time integrators. *International Journal for Numerical Methods in*
337 *Engineering* 2004; 60(1): 153–212. doi: <https://doi.org/10.1002/nme.958>
- 338 29. Fong W, Darve E, Lew A. Stability of asynchronous variational integrators. *Journal of Computational Physics* 2008;
339 227(18): 8367-8394. doi: <https://doi.org/10.1016/j.jcp.2008.05.017>
- 340 30. Focardi M, Mariano PM. Convergence of asynchronous variational integrators in linear elastodynamics. *International*
341 *Journal for Numerical Methods in Engineering* 2008; 75(7): 755-769. doi: <https://doi.org/10.1002/nme.2271>
- 342 31. Ryckman RA, Lew AJ. An explicit asynchronous contact algorithm for elastic body-rigid wall interaction. *International*
343 *Journal for Numerical Methods in Engineering* 2012; 89(7): 869-896. doi: <https://doi.org/10.1002/nme.3266>
- 344 32. Liu P, Yang JZ, Yuan C. Extended synchronous variational integrators for wave propagations on non-uniform meshes.
345 *Communications in Computational Physics* 2020; 28(2): 691–722. doi: <https://doi.org/10.4208/cicp.OA-2019-0167>
- 346 33. Thomaszewski B, Pabst S, Straßer W. Asynchronous Cloth Simulation. In: The 2008 International Conference on Computer
347 Graphics and Virtual Reality; 2008.
- 348 34. Pham K, Amor H, Marigo JJ, Maurini C. Gradient damage models and their use to approximate brittle fracture. *International*
349 *Journal of Damage Mechanics* 2011; 20(4): 618-652. doi: [10.1177/1056789510386852](https://doi.org/10.1177/1056789510386852)
- 350 35. Ren H, Zhuang X, Anitescu C, Rabczuk T. An explicit phase field method for brittle dynamic fracture. *Computers &*
351 *Structures* 2019; 217: 45-56. doi: <https://doi.org/10.1016/j.compstruc.2019.03.005>
- 352 36. Suh HS, Sun W. Asynchronous phase field fracture model for porous media with thermally non-equilibrated
353 constituents. *Computer Methods in Applied Mechanics and Engineering* 2021; 387: 114182. doi:
354 <https://doi.org/10.1016/j.cma.2021.114182>
- 355 37. Miehe C, Hofacker M, Welschinger F. A phase field model for rate-independent crack propagation: Robust algorithmic
356 implementation based on operator splits. *Computer Methods in Applied Mechanics and Engineering* 2010; 199(45): 2765-
357 2778. doi: [10.1016/j.cma.2010.04.011](https://doi.org/10.1016/j.cma.2010.04.011)
- 358 38. Amor H, Marigo JJ, Maurini C. Regularized formulation of the variational brittle fracture with unilateral con-
359 tact: Numerical experiments. *Journal of the Mechanics and Physics of Solids* 2009; 57(8): 1209-1229. doi:
360 <https://doi.org/10.1016/j.jmps.2009.04.011>
- 361 39. Liu Y, Cheng C, Ziaei-Rad V, Shen Y. A micromechanics-informed phase field model for brittle frac-
362 ture accounting for unilateral constraint. *Engineering Fracture Mechanics* 2021; 241: 107358. doi:
363 <https://doi.org/10.1016/j.engfracmech.2020.107358>

- 364 40. Wu JY, Nguyen VP, Zhou H, Huang Y. A variationally consistent phase-field anisotropic damage model for fracture. *Com-*
365 *puter Methods in Applied Mechanics and Engineering* 2020; 358: 112629. doi: <https://doi.org/10.1016/j.cma.2019.112629>
- 366 41. Marsden JE, West M. Discrete mechanics and variational integrators. *Acta Numerica* 2001; 10(10): 357-514. doi:
367 10.1017/S096249290100006X
- 368 42. Gerasimov T, De Lorenzis L. On penalization in variational phase-field models of brittle fracture. *Computer Methods in*
369 *Applied Mechanics and Engineering* 2019; 354: 990-1026. doi: <https://doi.org/10.1016/j.cma.2019.05.038>
- 370 43. Geelen RJ, Liu Y, Hu T, Tupek MR, Dolbow JE. A phase-field formulation for dynamic cohesive fracture. *Computer*
371 *Methods in Applied Mechanics and Engineering* 2019; 348: 680-711. doi: <https://doi.org/10.1016/j.cma.2019.01.026>
- 372 44. Wu JY. Robust numerical implementation of non-standard phase-field damage models for failure in solids. *Computer*
373 *Methods in Applied Mechanics and Engineering* 2018; 340: 767-797. doi: <https://doi.org/10.1016/j.cma.2018.06.007>
- 374 45. Farrell P, Maurini C. Linear and nonlinear solvers for variational phase-field models of brittle fracture. *International Journal*
375 *for Numerical Methods in Engineering* 2017; 109(5): 648-667. doi: <https://doi.org/10.1002/nme.5300>
- 376 46. Knuth DE. *The Art of Computer Programming*. Addison Wesley . 1998.
- 377 47. Song JH, Wang H, Belytschko T. A comparative study on finite element methods for dynamic fracture. *Computational*
378 *Mechanics* 2008; 42: 239-250. doi: 10.1007/s00466-007-0210-x
- 379 48. Ramulu M, Kobayashi AS. Mechanics of crack curving and branching – a dynamic fracture analysis. *International Journal*
380 *of Fracture* 1985; 27: 187-201. doi: <https://doi.org/10.1007/BF00017967>
- 381 49. Sharon E, Fineberg J. Microbranching instability and the dynamic fracture of brittle materials. *Physical Review B Condensed*
382 *Matter* 1996; 54(10): 7128-7139. doi: 10.1103/physrevb.54.7128
- 383 50. Schlüter A, Kuhn C, Müller R. Phase field approximation of dynamic brittle fracture. *Proceedings in Applied Mathematics*
384 *and Mechanics* 2014; 14(1): 143-144. doi: <https://doi.org/10.1002/pamm.201410059>
- 385 51. Liu G, Li Q, Msekh MA, Zuo Z. Abaqus implementation of monolithic and staggered schemes for quasi-
386 static and dynamic fracture phase-field model. *Computational Materials Science* 2016; 121: 35-47. doi:
387 <https://doi.org/10.1016/j.commatsci.2016.04.009>
- 388 52. Bobaru F, Zhang G. Why do cracks branch? A peridynamic investigation of dynamic brittle fracture. *International Journal*
389 *of Fracture* 2015; 196: 59-98. doi: 10.1007/s10704-015-0056-8
- 390 53. Mandal TK, Nguyen VP, Wu JY. Evaluation of variational phase-field models for dynamic brittle fracture. *Engineering*
391 *Fracture Mechanics* 2020; 235: 107169. doi: <https://doi.org/10.1016/j.engfracmech.2020.107169>
- 392 54. Kalthoff JF. Shadow optical analysis of dynamic shear fracture. *Optical Engineering* 1988; 27(10): 835 – 840. doi:
393 10.1117/12.7976772
- 394 55. Kalthoff JF. Modes of dynamic shear failure in solids. *International Journal of Fracture* 2000; 101(1): 1–31. doi:
395 <https://doi.org/10.1023/A:1007647800529>
- 396 56. Wang H, Xu Y, Huang D. A non-ordinary state-based peridynamic formulation for thermo-visco-plastic
397 deformation and impact fracture. *International Journal of Mechanical Sciences* 2019; 159: 336-344. doi:
398 <https://doi.org/10.1016/j.ijmecsci.2019.06.008>
- 399 57. Chu D, Li X, Liu Z. Study the dynamic crack path in brittle material under thermal shock loading by phase field modeling.
400 *International Journal of Fracture* 2017; 208: 115-130. doi: <https://doi.org/10.1007/s10704-017-0220-4>
- 401 58. Zhou S, Rabczuk T, Zhuang X. Phase field modeling of quasi-static and dynamic crack propagation:
402 COMSOL implementation and case studies. *Advances in Engineering Software* 2018; 122: 31-49. doi:
403 <https://doi.org/10.1016/j.advengsoft.2018.03.012>

- 404 59. Zhang Y, Ren H, Areias P, Zhuang X, Rabczuk T. Quasi-static and dynamic fracture modeling by the
405 nonlocal operator method. *Engineering Analysis with Boundary Elements* 2021; 133: 120-137. doi:
406 <https://doi.org/10.1016/j.enganabound.2021.08.020>
- 407 60. Park K, Paulino GH, Celes W, Espinha R. Adaptive mesh refinement and coarsening for cohesive zone model-
408 ing of dynamic fracture. *International Journal for Numerical Methods in Engineering* 2012; 92(1): 1-35. doi:
409 <https://doi.org/10.1002/nme.3163>
- 410 61. Tangella RG, Kumbhar P, Annabattula RK. Hybrid Phase Field Modelling of Dynamic Brittle Fracture and Implementation
411 in FEniCS. In: Krishnapillai S, R. V, Ha SK., eds. *Composite Materials for Extreme Loading* Springer Singapore; 2022;
412 Singapore: 15–24
- 413 62. Reddy SSK, Amirtham R, Reddy JN. Modeling fracture in brittle materials with inertia effects using the phase field method.
414 *Mechanics of Advanced Materials and Structures* 2021; 0(0): 1-16. doi: 10.1080/15376494.2021.2010289
- 415 63. Bourdin B, Francfort GA, Marigo JJ. The variational approach to fracture. *Journal of Elasticity* 2008; 91: 5-148. doi:
416 <https://doi.org/10.1007/s10659-007-9107-3>
- 417 64. Bleyer J, Roux-Langlois C, Molinari JF. Dynamic crack propagation with a variational phase-field model: Limiting
418 speed, crack branching and velocity-toughening mechanisms. *International Journal of Fracture* 2017; 204: 79-100. doi:
419 <https://doi.org/10.1007/s10704-016-0163-1>